PAPER

Check for updates

Low-temperature solution-processed SnO2 electron transport layer modified by oxygen plasma for planar perovskite solar cells†

Akshaiya Padmalatha Muthukrishnan,[a] Junyeoung Lee,[a] Jongbok Kim, [b] Chang Su Kim[c] and Sungjin Jo *[a]

SnO2 has attracted significant attention as an electron transport layer (ETL) because of its wide optical bandgap, electron mobility, and transparency. However, the annealing temperature of 180 °C–200 °C, as reported by several studies, for the fabrication of SnO2 ETL limits its application for flexible devices. Herein, we demonstrated that the low-temperature deposition of SnO2 ETL and further surface modification with oxygen plasma enhances its efficiency from 2.3% to 15.30%. Oxygen plasma treatment improves the wettability of the low-temperature processed SnO2 ETL that results in a larger perovskite grain size. Hence, oxygen plasma treatment effectively improves the efficiency of perovskite solar cells at a low temperature and is compatible with flexible applications.

1. Introduction

Among the next-generation solar cells, organic–inorganic hybrid perovskite solar cells (PSCs) have emerged as a nascent technology in recent years due to their high photoelectric power-conversion efficiency (PCE), low cost, and ease of fabrication. Intensive research on light-absorbing materials, electron transport layers (ETLs), and hole transport layers (HTLs) resulted in a drastic improvement in the PCE from 3.8% to 25.5% over the past decade.[1–6] Generally, n-i-p planar structures are employed in most state-of-the-art PSCs where the perovskite light-absorbing layer is sandwiched between the ETL and HTL.[7] Appropriate selection of the ETL plays a dominant role in determining the performance of PSCs by effectively extracting and transporting photogenerated electrons from the perovskite layer to the electrodes. Recently, extensive research has been focused on metal oxide-based ETLs, such as TiO2, SnO2, ZnO, InO3, and Nb2O5, for planar structure-based PSCs.[8–13]

Although most of the highly efficient PSCs employ TiO2 as the ETL, the high-temperature sintering process, low mobility, and instability under ultraviolet (UV) light limit its application

for flexible and commercial PSCs. In contrast, SnO2 has attracted attention as an excellent alternative to TiO2 because of its distinct advantages, such as its wide optical bandgap, high electron mobility, and good optical stability. It can be also processed at lower temperatures than TiO2,[14–17] and several studies have reported the fabrication of SnO2 ETL at annealing temperatures of 180 °C–200 °C.[18–21] However, the required fabrication temperature is still high and incompatible with most plastic substrates. To circumvent this problem, alternative annealing methods have been developed, such as UV, vacuum, and microwave-assisted annealing, to facilitate the formation of the metal oxide layer at low temperatures. For example, Xiao-dong Ren *et al.* used a UV ozone illumination to prepare a chlorinated SnO2 as ETL for PSC.[22,23] Huang *et al.* employed UV-assisted annealing of SnO2 film as a low-temperature ETL for PSCs.[24] In addition, Menghua *et al.* effectively prepared SnO2 ETL *via* an in-pulsed photonic annealing technique.[25] These low-temperature methodologies lead to the formation of SnO2 ETLs at a low temperature, but the device characteristics in these studies were lower than those obtained using thermally annealed SnO2. Therefore, there is a desperate need for an innovative precursor-to-metal oxide conversion strategy capable of breaking the alkoxy and hydroxyl groups to form a metal–oxide–metal network, thereby producing a high-quality SnO2 ETL at a low temperature.

In this study, we adopt a simple and effective oxygen plasma treatment on low-temperature deposited SnO2 (LT-SnO2) ETL. In this method, a sol–gel-coated SnO2 layer is activated by the highly reactive and energetic species in the plasma, which facilitates a rapid precursor-to-metal oxide conversion at a low temperature. The low-temperature SnO2 modified by oxygen plasma (LTP-SnO2) retains material properties comparable to

[a] School of Energy Engineering, Kyungpook National University, Daegu 41566, Republic of Korea. E-mail: sungjin@knu.ac.kr

[b] Department of Materials Science and Engineering, Kumoh National Institute of Technology, Gumi 39177, Republic of Korea

[c] Department of Advanced Functional Thin Films, Surface Technology Division, Korea Institute of Materials Science, 797 Changwondaero, Sungsan-Gu, Changwon, Gyeongnam 51508, Republic of Korea

† Electronic supplementary information (ESI) available: *J–V* curves of perovskite solar cells; XRD and XPS analysis of SnO2; XRD and SEM analysis of MAPbI3; contact angle images of water droplet on SnO2; device parameters of perovskite solar cells. See DOI: 10.1039/d1ra08946c

those of high-temperature annealed SnO_2 (HT-SnO_2). Therefore, the LTP-SnO_2 ETL-based PSCs show a significant improvement over LT-SnO_2 ETL-based PSCs. Moreover, surface modification with oxygen plasma improves the wettability of LT-SnO_2, which in turn increases the grain size of $CH_3NH_3PbI_3$ (MAPbI$_3$), resulting in reduced charge recombination at the grain boundaries. After undergoing plasma treatment, the PCE of PSC based on LT-SnO_2 and LTP-SnO_2 increases from 2.3% to 15.30%. Further, the open-circuit voltage (V_{oc}) of LT-SnO_2 based PSC increases rapidly from 0.34 to 1.06 V after plasma treatment, which indicates the suppression of charge recombination at the ETL/MAPbI$_3$ interface. This study demonstrates the efficacy of low-temperature fabrication of PSCs for future applications.

2. Materials and methods

2.1 Synthesis of SnO_2

Facile synthesis of SnO_2 sol–gel was carried out using the solution-processed method. $SnCl_2 \cdot 2H_2O$ was dissolved in ethanol to obtain a precursor solution with a concentration of 0.05 M. The solution was stirred at 1000 rpm for 24 h. Before the solution is spin-coated on a fluorine-doped tin oxide (FTO) substrate, it is filtered with a polytetrafluoroethylene filter to obtain a clear and homogeneous solution without any impurities. The reaction mechanism involved in the formation of SnO_2 during the synthesis process is given below.[26]

$$SnCl_2 \cdot 2H_2O + C_2H_5OH \rightarrow Sn(OH)_2 + C_2H_5Cl$$

$$Sn(OH)_2 \rightarrow SnO + H_2O$$

$$SnO \rightarrow SnO_2$$
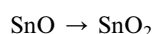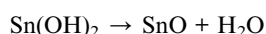
2.2 Fabrication of SnO_2 layer and perovskite solar cell

SnO_2 film is prepared by spin coating the above precursor solution on an FTO substrate at 2000 rpm for 30 s and then heated at a temperature of 200 °C and 150 °C for high-temperature and low-temperature annealing, respectively. Oxygen plasma treatment was performed on low-temperature annealed ETL at a radio frequency power of 20 W for 10 min immediately before coating the perovskite layer. The perovskite solar cell device was fabricated according to our previously reported work.[27]

2.3 Measurements

The surface morphology and topology of SnO_2 and MAPbI$_3$ layers were characterized using scanning electron microscopy (SEM; SU8220, Hitachi) and atomic force microscopy (AFM; NX20, Park System). The crystallographic changes were measured *via* X-ray diffractometer (XRD; Bruker AXS, D8-Discover) using Cu Kα excitation. X-ray photoelectron spectroscopy (XPS) analysis was carried out using a Quantera SXM (ULVAC-PHI) instrument. The steady-state photoluminescence (PL) spectra and time-resolved photoluminescence (TRPL) were

acquired using MicroTime-200 (Picoquant), which uses an inverted-type scanning confocal microscope. The photovoltaic characteristics of PSCs were measured under AM 1.5G illumination using Sol2A (Oriel). The contact-angle (CA) images and results were attained from CA-measuring equipment (GSX, SurfaceTech Co.).

3. Results and discussion

In our study, we employed a planar heterojunction (FTO/SnO_2/MAPbI$_3$/Spiro-OMeTAD/Ag) based PSC architecture. To investigate the effect of oxygen plasma treatment on the performance of PSCs based on LT-SnO_2, we fabricated three different sets of PSCs with the aforementioned structure. The main difference among the three sets is post-treatment of the SnO_2 layers. In the case of the pristine LT-SnO_2-based PSC, SnO_2 was only annealed at 150 °C, whereas oxygen plasma was directly performed on the LT-SnO_2 for the LTP-SnO_2-based PSC. For comparison, we also fabricated a conventional HT-SnO_2-based PSC by annealing SnO_2 at 200 °C.

Fig. 1 shows the current density–voltage curve (J–V curve) for champion cells based on LT-SnO_2, LTP-SnO_2, and HT-SnO_2. PSC fabricated using LT-SnO_2 generated a PCE of 2.27% with V_{oc} of 0.34 V, short-circuit current density (J_{sc}) of 18.44 mA cm^{-2}, and fill factor (FF) of 0.36. Fascinatingly, after oxygen plasma treatment on LT-SnO_2, the performance of PSC is drastically improved with PCE, V_{oc}, J_{sc}, and FF values of 15.30%, 1.06 V, 20.58 mA cm^{-2}, and 0.70, respectively. Moreover, the PSC based on LTP-SnO_2 has a higher PCE than that of the conventionally annealed HT-SnO_2-based PSC, 13.52%. The device parameters are listed in Table 1. The LT-SnO_2-based PSC exhibited inferior performance due to the incomplete precursor-to-metal oxide conversion affecting the interface between MAPbI$_3$ and ETL, as foreseen by the shallow slope of the J–V curve.[28] Plasma treatment effectively modifies the surface of LT-SnO_2, facilitating metal oxide formation and improving the growth property of the subsequent perovskite layer. This result indicates that it is possible to fabricate SnO_2 ETL at a low temperature using oxygen plasma.
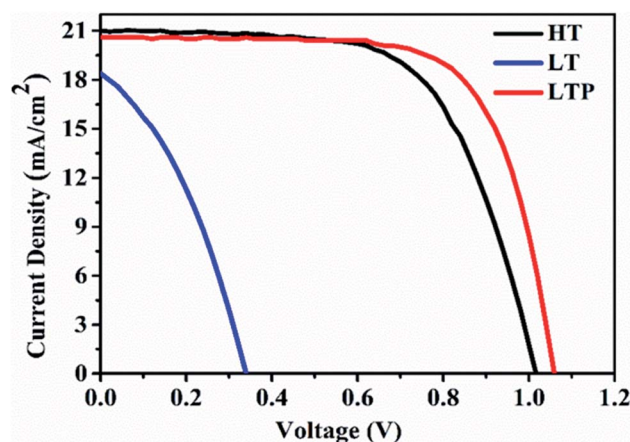

Fig. 1 J–V characteristics of the best performing PSCs fabricated with HT-, LT-, and LTP-SnO_2.

**Table 1** Photovoltaic performance parameters of the best performing PSCs

Device	J_{sc} (mA cm^{-2})	V_{oc} (V)	Fill factor	Efficiency (%)
HT-SnO$_2$	21.02	1.02	0.63	13.52
LT-SnO$_2$	18.44	0.34	0.36	2.27
LTP-SnO$_2$	20.58	1.06	0.70	15.30

A statistical distribution for all three types of PSC is obtained to investigate the reproducibility of the fabrication process, as shown in Fig. 2, and the corresponding device parameters are listed in Table S1.† The average PCE of the LTP-SnO$_2$-based PSC is 14.16%, which is higher than that of the LT-SnO$_2$- and HT-SnO$_2$-based PSCs. All the device parameters of the LTP-SnO$_2$-based PSC show smaller deviations, which indicate that oxygen plasma treatment is a consistent and reproducible process.

The above experimental results demonstrate that oxygen plasma treatment is sufficiently effective to improve the performance of LT-SnO$_2$-based PSCs. In addition, a series of experiments were conducted at various annealing temperatures ranging from 100 °C to 150 °C to ascertain that oxygen plasma treatment is also valid for lower annealing temperatures under 150 °C (Fig. S1 and Table S2†). The efficiency of the LT-SnO$_2$-based PSCs significantly increased, even at an annealing temperature of 100 °C, with oxygen plasma treatment, and the highest efficiency was obtained at 150 °C. Although the efficiency of LTP-SnO$_2$-based PSCs increased as the annealing temperature increased, it was confirmed that the oxygen plasma treatment was still effective in improving the efficiency of PSCs at much lower temperatures. Furthermore, the efficiency of the LTP-SnO$_2$ PSC annealed at 125 °C was comparable to that of HT-SnO$_2$ PSC, revealing that the fabrication temperature achieved with oxygen plasma treatment is compatible with most plastic substrates.

First, to elucidate the causes of enhancement in photovoltaic performance *via* oxygen plasma treatment, we investigated the compositional and structural changes in SnO$_2$ ETL by XPS, XRD, and AFM. As shown in Fig. S3,† XRD analysis was performed for LTP-, LT-, and HT-SnO$_2$. As expected, the SnO$_2$ layers are amorphous with no visible diffraction peaks, irrespective of post-treatment conditions, because a high temperature of 450 °C is required for the formation of the SnO$_2$ crystalline structure.[29,30] Fig. 3 shows the AFM images of HT-, LT-, and LTP-SnO$_2$. All the SnO$_2$ films based on different post-treatment conditions resulted in a uniform surface with a root-mean-square roughness value of ~34 nm. Oxygen plasma treatment on the SnO$_2$ surface does not significantly affect the surface morphology of SnO$_2$. However, oxygen plasma on LT-SnO$_2$ improved its hydrophilicity, as determined by CA measurement (Fig. S4†). The low surface energy of LT-SnO$_2$ (CA of 63.78°) reduces the uniform coverage of MAPbI$_3$ on its surface, which affects the performance of the PSC. The improved wettability of LTP-SnO$_2$ enhances the interface characteristics between the ETL and perovskite layer. Fig. 4 shows the XPS spectra of the Sn, O, and Cl peaks for the LT- and LTP-SnO$_2$ layers. Both LT- and LTP-SnO$_2$ films exhibited two peaks at binding energies of 487.3 and 495.7 eV corresponding to Sn 3d$_{5/2}$ and Sn 3d$_{3/2}$, as previously reported.[31] The single peak at 487.3 eV is assigned to the
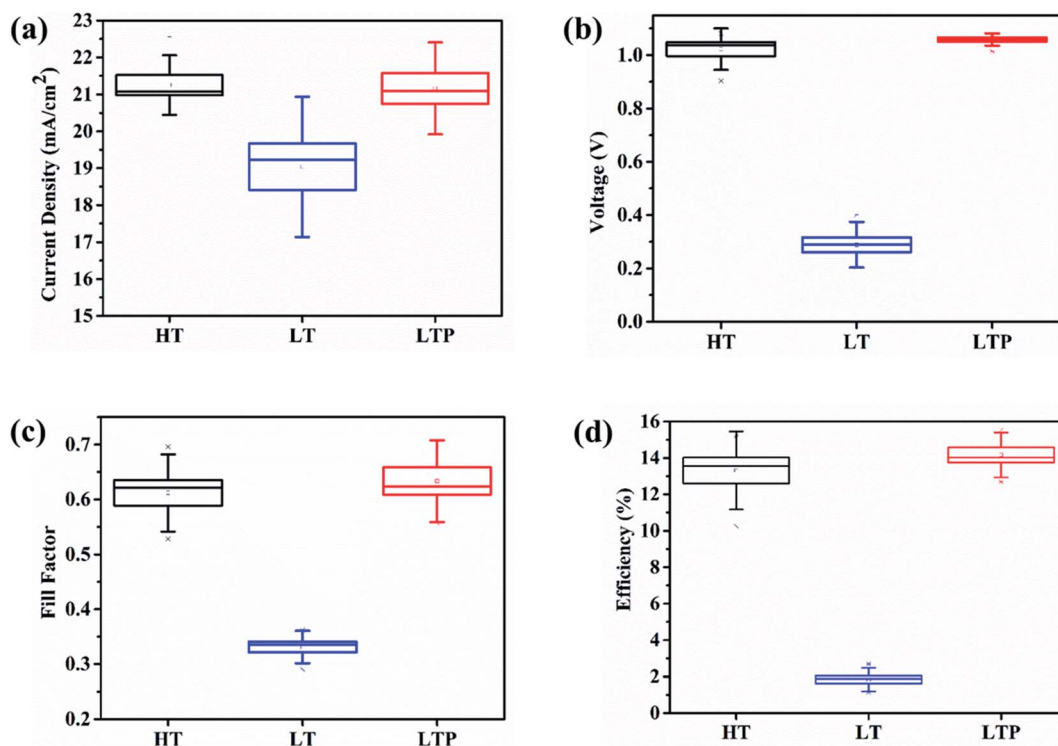
Fig. 2 Statistical distribution of PSCs fabricated with HT-, LT-, and LTP-SnO$_2$. (a) J_{sc} (b) V_{oc} (c) fill factor (d) efficiency.
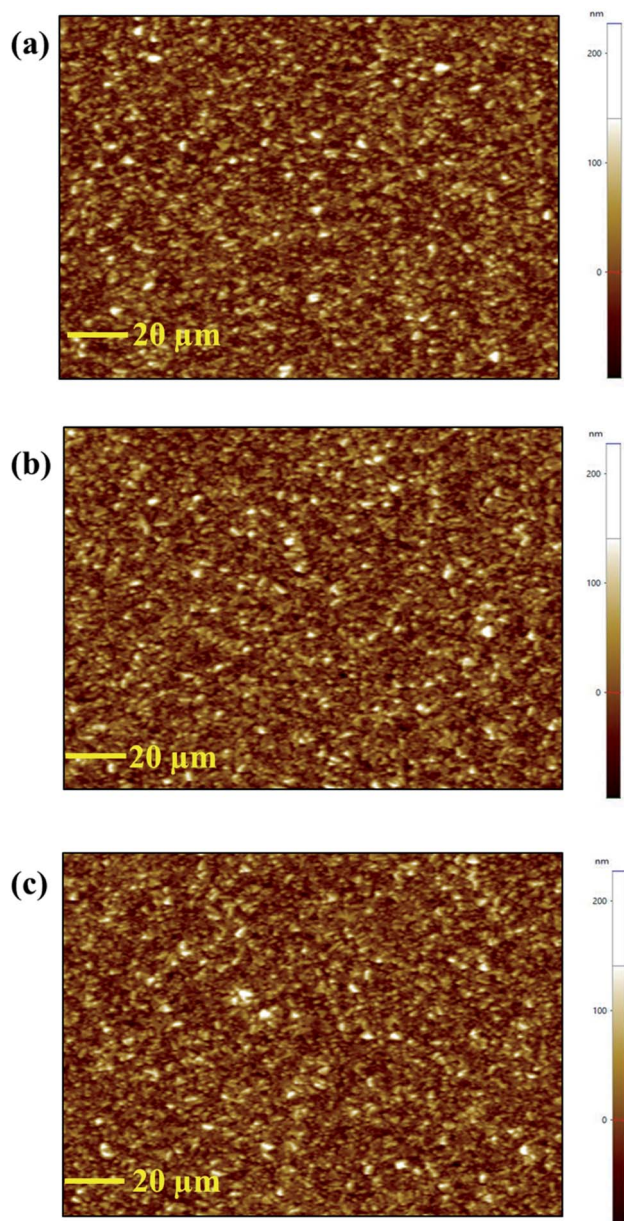
Fig. 3 AFM images of (a) HT-SnO₂, (b) LT-SnO₂ and (c) LTP-SnO₂.

Sn^{4+} oxidation state of SnO_2. However, there is no visible peak at the binding energy of 485.8 eV that corresponds to the Sn^{2+} oxidation state which indicates the formation of SnO. At a low temperature, the reaction involved in the formation of SnO_2 might occur *via* an indirect pathway that produces an intermediate product $Sn(OH)_2$ because of the reaction of $SnCl_2$ with C_2H_5OH as given in the above reaction equation. This intermediate product is converted into SnO which further reacts to form SnO_2.[32] Therefore, a single peak at the 487.3 eV reveals that SnO_2 begun to form at a low temperature of 150 °C. The XPS peak of O 1s were deconvoluted into two peaks, where a peak at a binding energy of 531.1 eV corresponds to the lattice oxygen atoms that confirms the formation of SnO_2.[24] The peak at the binding energy of 532.2 eV represents hydroxide species.[33] After

undergoing oxygen plasma, the –OH group of $LT-SnO_2$ decreased slightly, indicating that oxygen plasma helps in the breakage of the –OH bond and initiates the formation of SnO_2.[13] The most noticeable difference that arises in the XPS spectra from plasma treatment is the detection of Cl^-, as shown in Fig. 4b. The Cl^- peak originates from the utilization of $SnCl_2 \cdot 2H_2O$ precursor to fabricate the SnO_2 ETL. As can be observed, $LT-SnO_2$ has high-intensity Cl 2p peaks that indicate the presence of residual Cl^-. After oxygen plasma treatment, the Cl 2p level gradually decreased, representing the minimal presence of metal chloride precursor. This means that oxygen plasma improves the conversion of the precursor to metal oxide, as described in the above equation.

Second, to investigate the improvement in the performance of oxygen plasma-treated PSCs, the structural and morphological changes in the $MAPbI_3$ layer were examined. The XRD patterns of the $MAPbI_3$ layer on LT-, HT-, and $LTP-SnO_2$ are displayed in Fig. S5.† The samples based on different ETL conditions exhibit diffraction peaks at 14.08°, 20.0°, 23.54°, 24.5°, 28.4°, 31.9°, 34.9°, 40.5°, and 43.2° corresponding to the (110), (112), (211), (202), (220), (222), (312), (224), and (314) planes, respectively, which confirms the formation of a tetrahedral $MAPbI_3$ structure.[34] There are no noticeable differences in the crystalline nature of the $MAPbI_3$ layer for HT-, LT-, and $LTP-SnO_2$. This reveals that oxygen plasma treatment does not affect the crystalline nature of the perovskite layer. Fig. 5 and S7† show the top view SEM image and cross sectional SEM image of the perovskite film deposited on $LT-SnO_2$ and $LTP-SnO_2$. The surface morphology of $MAPbI_3$ on HT-, LT-, and $LTP-SnO_2$ is uniform, dense, and homogeneous with pinhole-free structures. The average grain size of the perovskite film for $LTP-SnO_2$ is 314.38 nm, which is greater than those of $HT-SnO_2$ and $LT-SnO_2$ with values of 280.33 and 255.68 nm, respectively. It is generally accepted that a $MAPbI_3$ grain size of 300–500 nm is beneficial for charge transportation on PSC.[16,35] The large grain size in $LTP-SnO_2$ is obtained because oxygen plasma improves the wettability of the surface, as indicated by the low CA. This small CA reduces the Gibbs free energy for heterogeneous nucleation, which assists the nucleation process that leads to improved grain size.[36] This improved grain size reduces the interface defect states that sequentially suppress the charge recombination at the grain boundaries, thus leading to improved PCE for oxygen plasma-treated PSCs. The reduced grain size in $LT-SnO_2$ is also responsible for its lower V_{oc}, as indicated by the J–V graph, because of the high charge trap sites within the grain boundaries.[15]

To further investigate the role of oxygen plasma treatment on the interfacial transfer kinetics between the ETL and perovskite layer, we analyzed the steady-state PL spectra and TRPL decay on the $HT-SnO_2/MAPbI_3$, $LT-SnO_2/MAPbI_3$, and $LTP-SnO_2/MAPbI_3$ films, as shown in Fig. 6. The peak at 770 nm corresponds to the fluorescence emission originating from the $MAPbI_3$ layer.[4] The PL intensity of perovskite on $LTP-SnO_2$ is strongly quenched compared to that of $MAPbI_3$ deposited on $HT-SnO_2$ and $LT-SnO_2$. This indicates that efficient electron extraction and transportation from $MAPbI_3$ to the $LTP-SnO_2$ layer subdues the nonradiative recombination at the interface.
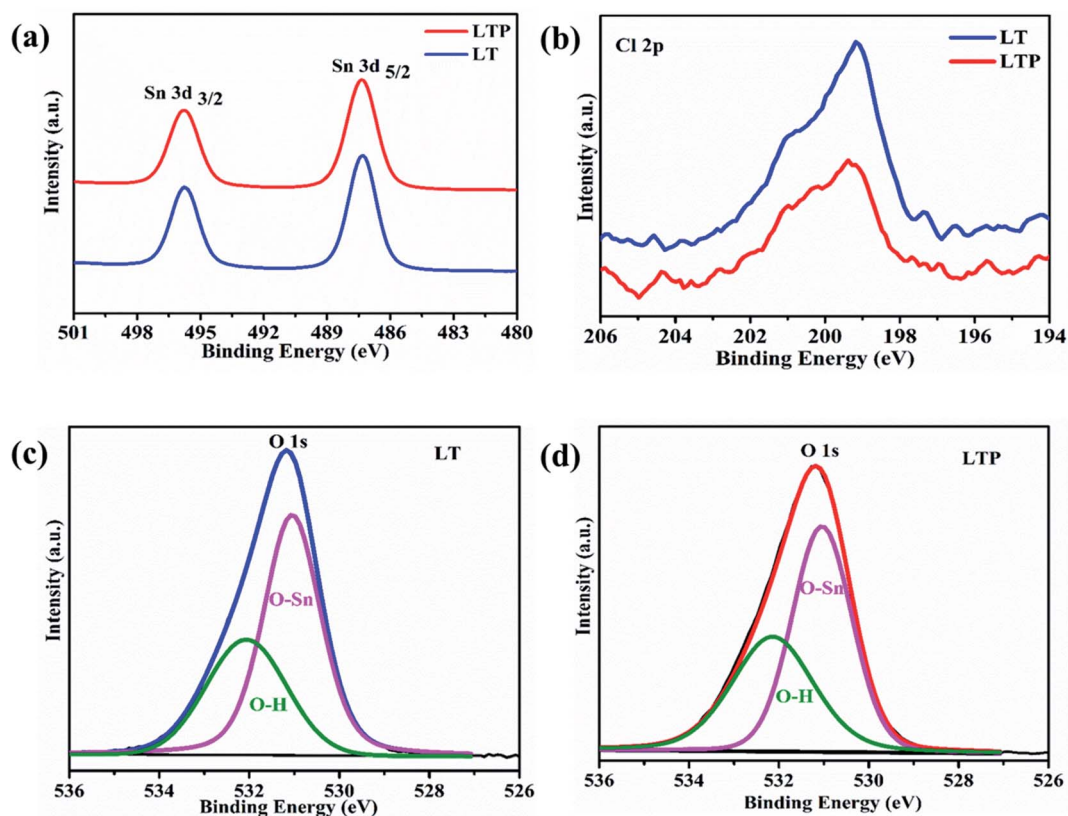
Fig. 4   XPS spectra of (a) Sn 3d, (b) Cl 2p from LT- and LTP-SnO$_2$. (c) and (d) O 1s from LT- and LTP-SnO$_2$, respectively.
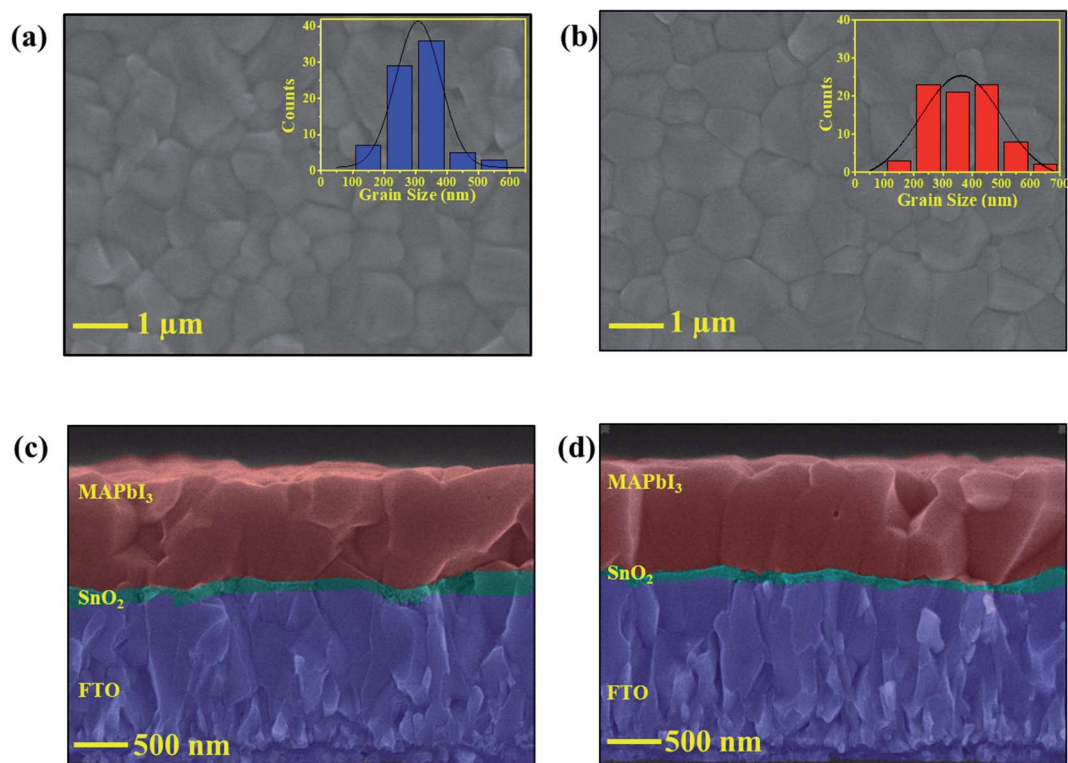

Fig. 5   Top view SEM images and grain size distribution histograms (inset) of MAPbI$_3$ deposited on (a) LT-SnO$_2$ and (b) LTP-SnO$_2$. Corresponding cross sectional SEM images of MAPbI$_3$ deposited on (c) LT-SnO$_2$ and (d) LTP-SnO$_2$.
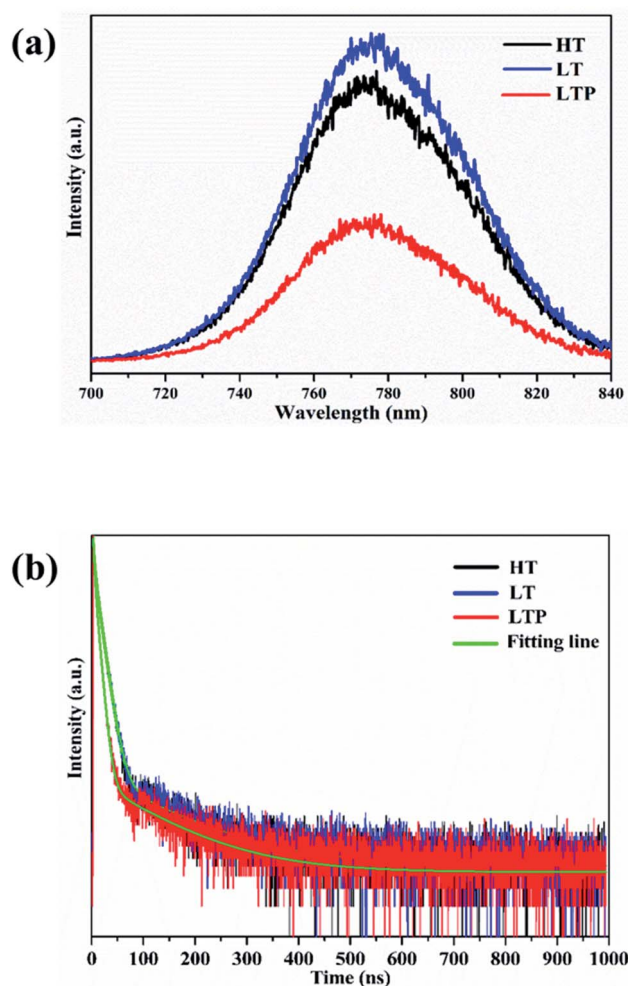
Fig. 6 (a) Steady state PL spectra and (b) TRPL spectra of MAPbI$_3$ deposited on HT-, LT-, and LTP-SnO$_2$.

Fig. 6b illustrates the TRPL decay profiles of the perovskite layer on the HT-SnO$_2$, LT-SnO$_2$, and LTP-SnO$_2$ samples. The corresponding τ values were determined by fitting the data with tri-exponential decay functions, and the values are represented in Table S3.† The value of τ_1, τ_2, and τ_3 correspond to the decay time of fast, intermediate, and slow component respectively. Fast decay components correspond to an effective charge extraction from perovskite to the ETL layer, whereas τ_2 and τ_3 represent the radiative recombination of free carriers.[37,38] In addition, the LTP-SnO$_2$ sample exhibits a low PL decay time (τ_1 = 2.28, τ_2 = 7.24) compared to LT-SnO$_2$ (τ_1 = 2.48, τ_2 = 11.5), indicating an effective electron transfer from the perovskite to ETL. The average recombination lifetime (τ_{avg}) is calculated using the equation below:

$$\tau_{avg} = \frac{\sum_i \text{Ampl}_i}{\sum_i \text{Ampl}_i} \frac{\tau_i^2}{\tau_i}$$

where, Ampl is the amplitude and τ denotes the PL lifetime. The average lifetime (τ_{avg}) of LTP-SnO$_2$ (15 ns) is less than that of LT-SnO$_2$ (18 ns), which indicates that the photoinduced electron

transfer from MAPbI$_3$ to LTP-SnO$_2$ is faster than transfers from MAPbI$_3$ to HT-SnO$_2$ and LT-SnO$_2$. The shortest lifetime of LTP-SnO$_2$ is related to its reduced charge trapping, back recombination, and ion accumulation at the ETL/MAPbI$_3$ interface.[28] The SEM and PL results confirm that oxygen plasma-treated SnO$_2$ ETL exhibits superior performance to LT-SnO$_2$ due to its better charge extraction efficiency and larger MAPbI$_3$ grain size.

To more accurately examine the differences in the carrier transport and recombination dynamics at SnO$_2$ ETL/MAPbI$_3$ interfaces, electrochemical impedance spectroscopy (EIS) is performed. Fig. 7 shows the Nyquist plot obtained by EIS for three different PSCs measured under the dark condition at a bias voltage of 0.9 V. The solid lines in the graph represent the fitted results of the experimental data based on the equivalent circuit model shown in Fig. 7c. The values of the fitted parameters are given in Table S4.† The EIS spectra of all three devices have one arc that represents the interfacial recombination resistance (R_{rec}), which is inversely proportional to the

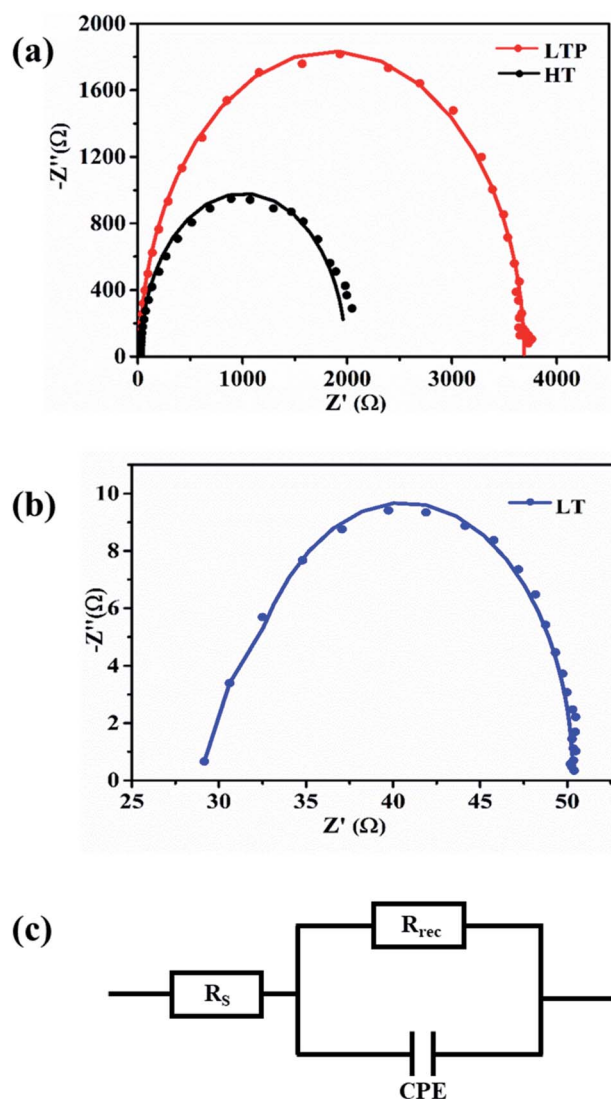Fig. 7 Nyquist plots of perovskite solar cells based on (a) HT-SnO$_2$ and LTP-SnO$_2$, (b) LT-SnO$_2$, (c) equivalent circuit model.

recombination rate of the charge carriers.[13,39] The larger arc of the LTP-SnO$_2$ corresponds to a higher R_{rec}, which indicates a smaller recombination constant (K_{rec}) in solar cells. The R_{rec} of LTP-SnO$_2$, 3669 Ω, is higher than those of HT-SnO$_2$ and LT-SnO$_2$, 1961 and 19.37 Ω, respectively. Higher R_{rec} values indicate that the device exhibits a low leakage current and reduced charge recombination at the ETL/MAPbI$_3$ interface.[40] In addition, we can interpolate the series resistance (R_s) from the EIS spectra at the starting point of the real part of the Nyquist plot.[9] The R_s value of LTP-SnO$_2$ is 19.69 Ω, which is lower than those of HT-SnO$_2$ and LT-SnO$_2$, which are 25.43 and 30.95 Ω, respectively. The only differences during device fabrication lie in the post-treatment of ETL; therefore, the small R_s and higher R_{rec} values of LTP-SnO$_2$ convey that oxygen plasma treatment on LT-SnO$_2$ is advantageous for efficient electron extraction, which is in agreement with the PL results. All the results based on PL, TRPL, and EIS are consistent with the PCE of the PSC for LTP-SnO$_2$ ETL.

Fig. 8 displays the J–V hysteresis of HT-SnO$_2$ and LTP-SnO$_2$ PSC by sweeping the forward and reverse scan directions. The value of the hysteresis index (HI) is determined from the following equation:[41]

$$\text{HI} = J_{RS}\,(0.8V_{oc}) - J_{FS}\,(0.8V_{oc})/J_{RS}\,(0.8V_{oc}),$$

where $J_{RS}\,(0.8V_{oc})$ and $J_{FS}\,(0.8V_{oc})$ correspond to photocurrent density at 80% of V_{oc} for the reverse and forward scan direction, respectively. The value of HI calculated from the above equation is found to be 0.26 and 0.16 for the HT-SnO$_2$ and LTP-SnO$_2$ PSCs, respectively A small value of HI is beneficial for solar cells, as this indicates a low hysteresis. The origin of HI in PSC is multifactored, as it can be attributed to either charge accumulation at the interface or other reasons, such as ion migration in MAPbI$_3$.[7] Therefore, the low HI for LTP-SnO$_2$ is mainly due to the low charge accumulation at the interface of ETL/MAPbI$_3$, as evidenced by previous TRPL results that show a low τ_{avg} value. It was also reported that the large grain size of MAPbI$_3$ also reduces HI.[41] Because LTP-SnO$_2$ has a larger grain size, it offers
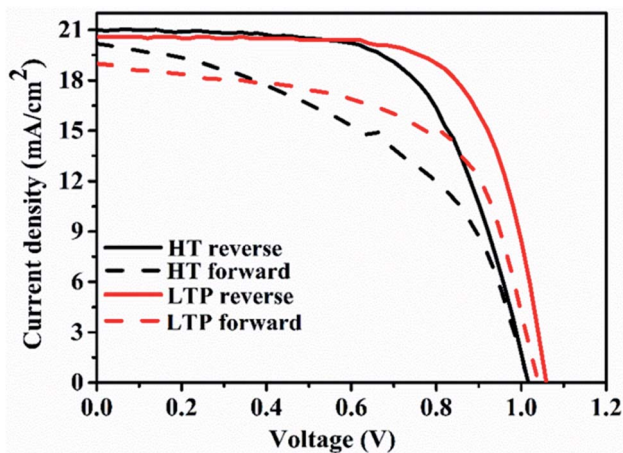
a low HI value. Thus, all the facts described above affirm the positive and essential role of oxygen plasma treatment in modifying the interfacial properties between the ETL and MAPbI$_3$, thereby enhancing the performance of PSCs.

4. Conclusion

Interface engineering of a low-temperature deposited SnO$_2$ film surface using oxygen plasma treatment improves the performance of PSCs. Oxygen plasma improves the conversion of the precursor-to-metal oxide layer. This effectively improves the hydrophilicity of LT-SnO$_2$, which enhances the surface coverage of the MAPbI$_3$ layer. The increased MAPbI$_3$ grain size of LTP-SnO$_2$ resulted in an improvement in V_{oc} from 0.34 V to 1.06 V after plasma treatment. Surface treatment by oxygen plasma does not affect the structural properties of the perovskite layer that is deposited on the top but leads to efficient electron extraction from the perovskite layer to the ETL. Further oxygen plasma effectively increased the recombination resistance at the ETL/perovskite interface and led to an efficiency of 15.30%. In this work, we studied the impact of oxygen plasma treatment in the structural, compositional, and morphological behaviors of SnO$_2$ and MAPbI$_3$. The results indicate that oxygen plasma treatment is effective for fabricating SnO$_2$-based PSCs for future flexible applications.

Author contributions

The manuscript was written through contributions of all authors. All authors have given approval to the final version of the manuscript.

Conflicts of interest

The authors declare no competing financial interest.

Acknowledgements

References

1 J. Jeong, M. Kim, J. Seo, H. Lu, P. Ahlawat, A. Mishra, Y. Yang, M. A. Hope, F. T. Eickemeyer, M. Kim, Y. J. Yoon, I. W. Choi, B. P. Darwich, S. J. Choi, Y. Jo, J. H. Lee, B. Walker, S. M. Zakeeruddin, L. Emsley, U. Rothlisberger, A. Hagfeldt, D. S. Kim, M. Grätzel and J. Y. Kim, *Nature*, 2021, **592**, 381–385.

2 H. Lu, A. Krishna, S. M. Zakeeruddin, M. Grätzel and A. Hagfeldt, *iScience*, 2020, **23**, 1–14.

3 L. Xiong, J. Li, F. Ye, H. Wang, Y. Guo, X. Ming, Q. Chen, S. Zhang, R. Xie, Z. Chen, Y. Lv, G. Hu, Y. He and G. Fang, *Adv. Funct. Mater.*, 2021, **31**, 2–11.

Fig. 8 J–V characteristics of PSCs based on HT- and LTP-SnO$_2$ in different scan directions.

4 C. Chen, Y. Jiang, J. Guo, X. Wu, W. Zhang, S. Wu, X. Gao, X. Hu, Q. Wang, G. Zhou, Y. Chen, J. M. Liu, K. Kempa and J. Gao, *Adv. Funct. Mater.*, 2019, **29**, 1–9.

5 X. Yin, Z. Song, Z. Li and W. Tang, *Energy Environ. Sci.*, 2020, **13**, 4057–4086.

6 S. Mabrouk, B. Bahrami, H. Elbohy, K. M. Reza, A. Gurung, M. Liang, F. Wu, M. Wang, S. Yang and Q. Qiao, *InfoMat*, 2020, **2**, 928–941.

7 M. Shekargoftar, J. Pospisil, M. Kratochvíl, J. Vida, P. Souček and T. Homola, *Energy Technol.*, 2021, **9**(5), 2001076.

8 P. F. Méndez, S. K. M. Muhammed, E. M. Barea, S. Masi and I. Mora-Seró, *Sol. RRL*, 2019, **3**(9), 1900191.

9 J. Song, E. Zheng, X. F. Wang, W. Tian and T. Miyasaka, *Sol. Energy Mater. Sol. Cells*, 2016, **144**, 623–630.

10 A. S. R. Bati, M. Hao, T. J. Macdonald, M. Batmunkh, Y. Yamauchi, L. Wang and J. G. Shapter, *Small*, 2021, **17**, 1–9.

11 J. Ma, J. Su, Z. Lin, L. Zhou, J. He, J. Zhang, S. Liu, J. Chang and Y. Hao, *Nano Energy*, 2020, **67**, 104241.

12 C. Zhang, Y. Shi, S. Wang, Q. Dong, Y. Feng, L. Wang, K. Wang, Y. Shao, Y. Liu and S. Wang, *J. Mater. Chem. A*, 2018, **6**, 17882–17888.

13 H. B. Lee, N. Kumar, M. M. Ovhal, Y. J. Kim, Y. M. Song and J. W. Kang, *Adv. Funct. Mater.*, 2020, **30**, 1–12.

14 X. Huang, Z. Hu, J. Xu, P. Wang, L. Wang, J. Zhang and Y. Zhu, *Sol. Energy Mater. Sol. Cells*, 2017, **164**, 87–92.

15 M. Park, J. Y. Kim, H. J. Son, C. H. Lee, S. S. Jang and M. J. Ko, *Nano Energy*, 2016, **26**, 208–215.

16 N. Zhu, X. Qi, Y. Zhang, G. Liu, C. Wu, D. Wang, X. Guo, W. Luo, X. Li, H. Hu, Z. Chen, L. Xiao and B. Qu, *ACS Appl. Energy Mater.*, 2019, **2**, 3676–3682.

17 J. Song, E. Zheng, J. Bian, X. F. Wang, W. Tian, Y. Sanehira and T. Miyasaka, *J. Mater. Chem. A*, 2015, **3**, 10837–10844.

18 W. Ke, G. Fang, Q. Liu, L. Xiong, P. Qin, H. Tao, J. Wang, H. Lei, B. Li, J. Wan, G. Yang and Y. Yan, *J. Am. Chem. Soc.*, 2015, **137**, 6730–6733.

19 E. H. Anaraki, A. Kermanpur, L. Steier, K. Domanski, T. Matsui, W. Tress, M. Saliba, A. Abate, M. Grätzel, A. Hagfeldt and J. P. Correa-Baena, *Energy Environ. Sci.*, 2016, **9**, 3128–3134.

20 G. Murugadoss, H. Kanda, S. Tanaka, H. Nishino, S. Ito, H. Imahoric and T. Umeyama, *J. Power Sources*, 2016, **307**, 891–897.

21 X. Ren, D. Yang, Z. Yang, J. Feng, X. Zhu, J. Niu, Y. Liu, W. Zhao and S. F. Liu, *ACS Appl. Mater. Interfaces*, 2017, **9**, 2421–2429.

22 X. Ren, Y. Liu, D. G. Lee, W. Bin Kim, G. S. Han, H. S. Jung and S. (Frank) Liu, *InfoMat*, 2020, **2**, 401–408.

23 B. Kan, Y. Kan, L. Zuo, X. Shi and K. Gao, *InfoMat*, 2021, **3**, 175–200.

24 L. Huang, X. Sun, C. Li, J. Xu, R. Xu, Y. Du, J. Ni, H. Cai, J. Li, Z. Hu and J. Zhang, *ACS Appl. Mater. Interfaces*, 2017, **9**, 21909–21920.

25 M. Zhu, W. Liu, W. Ke, S. Clark, E. B. Secor, T. Bin Song, M. G. Kanatzidis, X. Li and M. C. Hersam, *J. Mater. Chem. A*, 2017, **5**, 24110–24115.

26 V. H. Tran, R. B. Ambade, S. B. Ambade, S. H. Lee and I. H. Lee, *ACS Appl. Mater. Interfaces*, 2017, **9**, 1645–1653.

27 J. Nam, I. Nam, E. J. Song, J. D. Kwon, J. Kim, C. S. Kim and S. Jo, *Nanomaterials*, 2019, **9**, 1–10.

28 A. S. Subbiah, N. Mathews, S. Mhaisalkar and S. K. Sarkar, *ACS Energy Lett.*, 2018, **3**, 1482–1491.

29 M. F. M. Noh, M. F. Soh, C. H. Teh, E. L. Lim, C. C. Yap, M. A. Ibrahim, N. A. Ludin and M. A. M. Teridi, *Sol. Energy*, 2017, **158**, 474–482.

30 O. Kassem, M. Saadaoui, M. Rieu and J.-P. Viricelle, *Proceedings*, 2017, **1**, 622.

31 R. G. Motsoeneng, I. Kortidis, S. S. Ray and D. E. Motaung, *ACS Omega*, 2019, **4**, 13696–13709.

32 M. F. Mohamad Noh, N. A. Arzaee, J. Safaei, N. A. Mohamed, H. P. Kim, A. R. Mohd Yusoff, J. Jang and M. A. Mat Teridi, *J. Alloys Compd.*, 2019, **773**, 997–1008.

33 Y. Gao, Y. Masuda and K. Koumoto, *Langmuir*, 2004, **20**, 3188–3194.

34 J. Nam, J. H. Kim, C. S. Kim, J. D. Kwon and S. Jo, *ACS Appl. Mater. Interfaces*, 2020, **12**, 12648–12655.

35 B. Liu, S. Wang, Z. Ma, J. Ma, R. Ma and C. Wang, *Appl. Surf. Sci.*, 2019, **467–468**, 708–714.

36 D. Yang, R. Yang, K. Wang, C. Wu, X. Zhu, J. Feng, X. Ren, G. Fang, S. Priya and S. (Frank) Liu, *Nat. Commun.*, 2018, **9**, 3239.

37 Y. Liu, H. Lu, J. Niu, H. Zhang, S. Lou, C. Gao, Y. Zhan, X. Zhang, Q. Jin and L. Zheng, *AIP Adv.*, 2018, **8**(9), 095108.

38 J. Xing, C. Zhao, Y. Zou, W. Kong, Z. Yu, Y. Shan, Q. Dong, D. Zhou, W. Yu and C. Guo, *Light: Sci. Appl.*, 2020, **9**, 111.

39 Y. Li, C. Feng, H. Cheng and Z. S. Wang, *Sol. RRL*, 2018, **2**, 1–8.

40 R. Xu, Y. Li, S. Feng, J. Wang, J. Zhang, X. Zhang, C. Bian, W. Fu, Z. Li and H. Yang, *J. Mater. Sci.*, 2020, **55**, 5681–5689.

41 H.-S. Kim and N.-G. Park, *J. Phys. Chem. Lett.*, 2014, **5**, 3434.